Carbon Trends 15 (2024) 100348

Contents lists available at ScienceDirect

Carbon Trends

journal homepage: www.elsevier.com/locate/cartre

Synthesis and dynamics of PtSi nanoparticles on a carbon nanofilm by *in-situ* TEM Joule heating

Simon Hettler [a,b,*], Raul Arenal [a,b,c,*]

[a] Instituto de Nanociencia y Materiales de Aragón (INMA), Universidad de Zaragoza, Zaragoza, Spain
[b] Laboratorio de Microscopías Avanzadas (LMA), Universidad de Zaragoza, Zaragoza, Spain
[c] ARAID Foundation, Zaragoza, Spain

ARTICLE INFO

Keywords:
In-situ transmission electron microscopy
Amorphous carbon
Nanoparticle synthesis
Joule heating
Platinum silicide

ABSTRACT

In-situ transmission electron microscopy has evolved to be a unique technique to study process dynamics down to the atomic scale. Here, we show that *in-situ* Joule heating of carbon nanofilms facilitates the investigation of the nucleation, annealing, diffusion and evaporation of PtSi nanoparticles in a controlled way. The nanoparticles form from Pt-based hydrocarbon molecules and silicon oxide present on the amorphous carbon nanofilm. The *in-situ* transmission electron microscopy approach permits shedding light on the interaction between the nanoparticles and the carbon support, crucial information when aiming for stable catalytic applications. The method is versatile, allows reaching very high temperatures and could be applied to study many different combinations of bimetallic and even multimetallic high-entropy alloy nanoparticles.

1. Introduction

Understanding and controlling the synthesis of metallic and alloyed nanoparticles (NPs) is crucial for a successful application [1,2]. For a high catalytic activity, small, multimetallic NPs, also called high-entropy alloys, have shown to be a highly promising approach [3–5]. Within the area of bimetallic NPs, transition metal silicides, such as platinum silicide [6–8], are promising for catalytic applications due to their interesting electrical properties [9]. Often, the NPs are desired on a carbon-based substrate, which can be obtained directly by pyrolisis of metal-containing precursors on carbon compounds. A rapid increase of the synthesis temperature of precursor and substrate to 2000-3000 K for a short time (μs to ms) by either micro-wave assisted heating, Joule heating or laser has proven an efficient means for NP synthesis [10–15]. Transmission electron microscopy (TEM) is an important technique to analyze the obtained NPs, giving chemical and structural information down to the nanoscale. Using dedicated sample holders, *in-situ* TEM can be a way to study the NP synthesis dynamics [16–18] as well as the interaction with the (carbon) support materials, which is crucial when aiming for long-term stability of the NPs under application-relevant catalytic conditions or confinement approaches [19,20]. However, the preparation of *in-situ* TEM samples for the promising approach to study the on-carbon synthesis by Joule heating [16] remains challenging.

Amorphous carbon (aC) nanofilms have a long history as sample support or physical phase plate [21–25] for TEM, even before nanotechnology emerged at the end of the last century. A large variety of materials can be described as “amorphous carbon”, here we refer to films prepared under high-vacuum conditions by physical vapor deposition techniques. Such films are disordered, typically exhibit approximately 70% of sp^2 bonds, contain up to 10 at% of oxygen and negligible amounts of nitrogen [26]. aC nanofilms with a thickness below 20 nm are employed on a day-to-day basis in TEM as they allow high-resolution studies.

Following the investigation of the *in-situ* TEM reduction of graphene oxide [27], we have investigated the pyrolisis of such aC nanofilms by Joule heating. Although a recently developed transfer method permits the reproducible preparation of nanomaterial specimens for electrical *in-situ* TEM studies with minimum damage and contamination [28], even a minute amount of (semi-)metallic non-carbon atoms is sufficient to observe them forming NPs during the pyrolisis experiment. After this serendipitous observation, we investigated in detail the NP formation and found that the aC film permits such investigations in a controlled way and without limitation of the microscopes’ capabilities, being a methodological improvement compared to previous studies [16]. As an example experiment, we describe the dynamical evolution of PtSi NPs during Joule heating of aC nanofilms including nucleation, agglomeration, annealing, diffusion and evaporation.

* Corresponding authors.
E-mail addresses: hettler@unizar.es (S. Hettler), arenal@unizar.es (R. Arenal).

https://doi.org/10.1016/j.cartre.2024.100348
Received 10 January 2024; Received in revised form 28 February 2024; Accepted 22 March 2024
Available online 28 March 2024

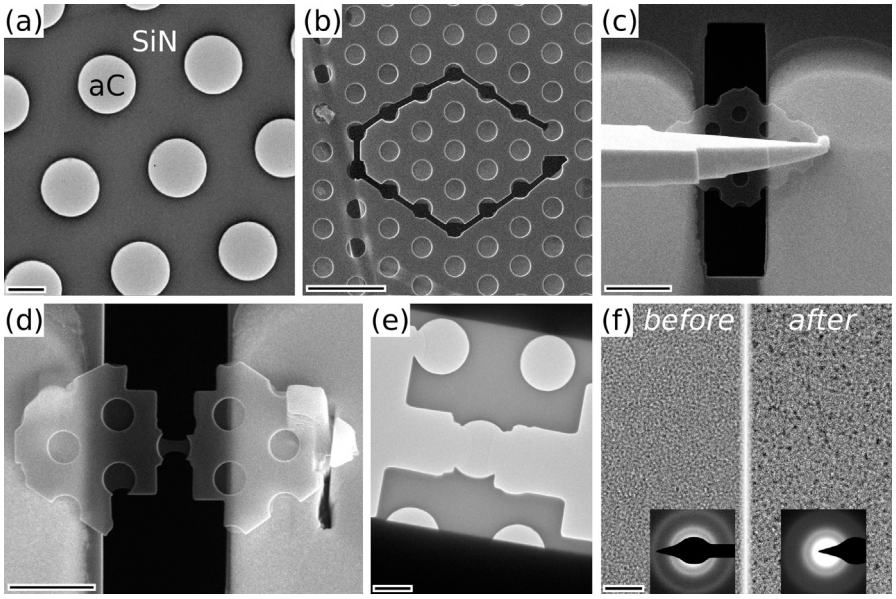

Fig. 1. Overview of the sample preparation. (a) TEM image of the aC nanofilm suspended on a holey SiN_x membrane. (b) SEM image of the same membrane and aC nanofilm after cutting by FIB. (c) SEM image of the membrane with aC nanofilm held by the microneedle above the contacts of the *in-situ* microchip. (d) SEM and (e) TEM images of the final device. (f) Comparison of defocused high-resolution TEM images and SAED patterns of the aC nanofilm before (left) and after (right) the transfer process. Scale bars are (a, e) 500 nm, (b, c) 3 μm, (d) 2 μm and (f) 9 nm. SAED patterns in (f) have a width of 20 nm^{-1}.

2. Materials and methods

2.1. Transmission electron microscopy techniques

The major part of the *in-situ* transmission electron microscopy (TEM) studies were conducted in an aberration-corrected (image) Titan^3 (Thermo Fisher Scientific) operated at 80 keV. Selected-area electron diffraction (SAED) patterns were acquired under parallel illumination. The SA apertures were also used to acquire electron energy-loss spectroscopy (EELS) data under parallel illumination in diffraction mode. The complete energy-loss range up to 600 eV was acquired with an acceptance angle of 19.7 mrad with a Gatan Image Filter (GIF) Tridiem 863 at a dispersion of 0.2 eV/channel. The energy axis of the EEL spectra has been calibrated by setting the onset of the carbon K edge to 282 eV. All EELS data throughout the experiment were acquired under identical illumination conditions (illuminated area of 1.2 μm), allowing a quantitative comparison of the intensities. Quantification of the Si L, the C K and the O K edges was done by integration of background-subtracted spectra (power-law) in a 30 eV window and theoretical cross sections [29]. The dose rate for SAED and EELS data acquisition was 10 $e^-Å^{-2}s^{-1}$ and was limited to approximately 200 $e^-Å^{-2}s^{-1}$ for the high-resolution (HR) imaging prior to nucleation. After nucleation, the dose rate was slightly increased to better resolve the crystal structure of the NPs. Damage inflicted on the sample by the electron beam could not be detected. TEM image series were acquired during the application of electrical current every 4 seconds with an Ultrascan 1000 CCD camera (Gatan).

For additional spatially-resolved chemical analysis, a second aberration-corrected (probe) Titan Low-Base (Thermo Fisher Scientific) with a high-brightness gun (X-FEG) operated at 80 keV was used. Energy-dispersive X-ray spectroscopy (EDX) was performed with an Oxford Instruments Ultim X-MaxN 100TLE detector and EELS in STEM mode (convergence angle 25 mrad) with a GIF Tridiem 865 at an acceptance angle of 68 mrad. EDX data was quantified with the Aztec software (Oxford Instruments) and theoretical k factors. EELS data was analyzed in a custom program written for Matlab (The Mathworks).

In-situ TEM experiments were conducted with a DENSsolution Wildfire *in-situ* sample holder (4 pins) and custom microchips (*vide infra*). Electrical current was applied to the aC nanofilm (denoted as I_{aC} in the following) using a Keithley 2450 SourceMeter (Tektronix). The current ramps were performed without delay in static mode, the readout time per measurement point is approximately 140 ms in the used current range.

2.2. Sample preparation

The aC nanofilm was prepared by electron-beam physical vapor deposition of a graphite target (PVD75, Lesker) on a freshly cleaved muscovite mica substrate. The aC nanofilm then was transferred to the back side of a carbon-coated holey silicon nitride (SiN_x) TEM grid (PELCO) by a water-based floating process. We used two grids with different diameters of the holes, one with multiple diameters between 70 and 1250 nm and a second one with equally-sized holes with 2.5 μm diameter. The thickness of the aC nanofilm was determined to be 10 nm from a cross-section TEM lamella prepared from a simultaneously coated Si wafer.

Following a recently described support-based transfer process [28], the aC nanofilm suspended on the SiN_x TEM grid was transferred to a custom *in-situ* microchip (*vide infra*) by a Ga^+ focused ion beam (FIB). Fig. 1 describes this process starting from the aC nanofilm suspended on the holey SiN_x support (hole diameter 900 nm) seen in a transmission electron microscope (Fig. 1a). A piece of the SiN_x support with aC nanofilm is cut free by FIB and transferred to the electrical contacts of the *in-situ* microchip with the help of a microneedle (Fig. 1b, c). Contacting is achieved by FIB-induced deposition of a Pt-based precursor ($C_5H_4CH_3Pt(CH_3)_3$). Finally, the SiN_x support is removed by FIB so that the aC nanofilm is the only bridge between the electrical contacts (Fig. 1d, e). In the example shown in Fig. 1, an observable amount of the Pt/C-based precursor gas was deposited on the aC nanofilm as seen in the defocused TEM image after the transfer (Fig. 1f). In addition to the Pt/C molecules, a minor amount of Ga is implanted in the film, which however could not be detected by spectroscopic techniques. The aC structure is conserved as shown by the SAED patterns and the comparison of EEL spectra before and after the transfer (Figure S1 in the supplementary information (SI)).

A second *in-situ* sample was prepared similarly with the identical film suspended on a SiN_x grid with larger hole diameters (2.5 μm), which is described in Figure S2 (SI). In this specimen, Pt contamination

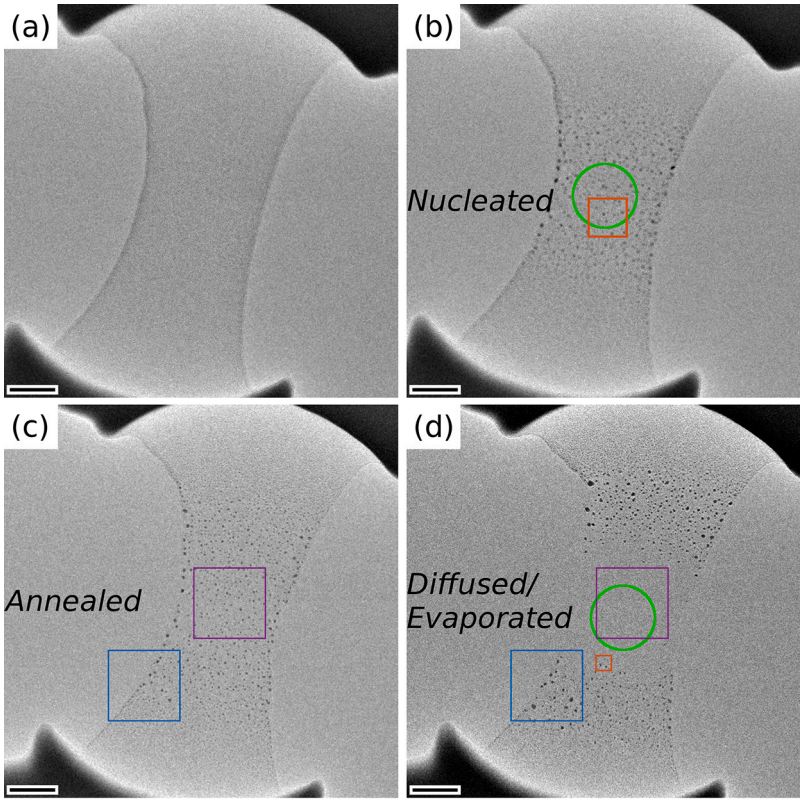

Fig. 2. TEM images of specimen (a) before *in-situ* experiment, (b) after NP nucleation, (c) after NP annealing at $I_{aC} = 40$ μA and (d) after NP diffusion/evaporation. Green circles in (b) and (d) indicate acquisition locations for SAED patterns displayed in Figs. 5b and 8b, respectively. Orange square in (b) indicates the area of the HRTEM image in Fig. 5c and blue and purple frames in (c) and (d) indicate positions of the TEM image series in Fig. 7. The small orange frame in (d) indicates the position of the TEM image series shown in Fig. 8a. Scale bar is 90 nm.

was strongly reduced and we therefore focus on the specimen described in Fig. 1 in this manuscript as it allows to better illustrate the formation of the NPs.

The custom *in-situ* microchips were fabricated in-house from a p-doped Si wafer double-side coated with 1 μm low-stress SiN_x as described in detail elsewhere [28]. The chips contain two electrodes and a heating element on a SiN_x membrane. The on-chip heating element was calibrated by measuring the Al plasmon energy by EELS in dependence of the applied heating current, however, as the individual chips can differ slightly between each other and the resistance is measured only in a two-terminal setup, the temperature can only be approximated.

3. *In-situ* synthesis and dynamics of Pt/Si nanoparticles

This article presents results mainly obtained from the *in-situ* experiment conducted with the specimen described in Fig. 1. Data was obtained on both the NPs' synthesis and the graphitization of the aC, but here we focus on the NPs and their interaction with the aC. The results on the evolution of the carbon structure will be presented together with additional samples in more detail in a separate article.

The *in-situ* experiment was composed of five phases:

1. Pre-heating: Heating of the sample up to approximately 250 °C using the on-chip heating element.
2. NP nucleation: Application of electrical current ramps with increasing maximum currents up to $I_{aC} = 50$ μA.
3. NP annealing: Application of a constant electrical current of $I_{aC} = 40$ μA.
4. NP diffusion/evaporation: Application of an electrical current ramp from $I_{aC} = 40$ to 50 μA.
5. 2nd annealing: Application of an electrical current ramp from $I_{aC} = 44$ to 46 μA.

Figs. 2-4 give an overview of the experiment. Fig. 2 shows TEM images of (a) the initial state of the aC nanofilm after transfer to the *in-situ* chip, (b) after NP nucleation, (c) after annealing and (d) after NP diffusion/evaporation. The rounded black parts at top and bottom of the images are the borders of the SiN_x membrane, which sustains the free-standing aC nanofilm. The dark spots that first appear in (b) correspond to PtSi NPs, as discussed in detail in this section. The electrical measurements during steps 2-5 are shown in Fig. 3. EELS data was acquired at different steps of the *in-situ* experiment and the spectra are shown in Fig. 4 including the low-loss region and the core-loss regions of the Si L, C K and O K edges. The overall decrease in intensity of all the spectra during the experiment is evident, the details will be discussed throughout the manuscript.

3.1. Initial state and pre-heating

During the transfer of the aC nanofilm to the *in-situ* microchip, a small amount of the precursor gas (hydrocarbonated Pt molecules) used for contacting the film to the contact pads was deposited on the aC nanofilm by secondary electrons/ions generated during the transfer process. Such focused-ion or electron-beam deposits typically contain a high amount of carbon of up to 80% [30], especially for low electron/ion doses, which was the case for the presented sample. These deposits are not visible in a focused TEM image but become visible with slight defocus (Fig. 1f). The clusters have a size of below 1 nm in diameter and the density of Pt atoms is estimated by counting the clusters to be below 1 atom per nm^2 for a Pt:C ratio of 1:3 in the deposits. Assuming a low estimate for the density of aC of 1 g cm^{-3} [31], the number of C atoms in a 10 nm thick film is approximately 500 atoms per nm^2, leading to a Pt:C ratio of <1:500. In addition to the Pt-based contamination inflicted during the sample preparation, the aC nanofilm exhibits a contamination by SiO_x stemming from the mica substrate. Quantifi-

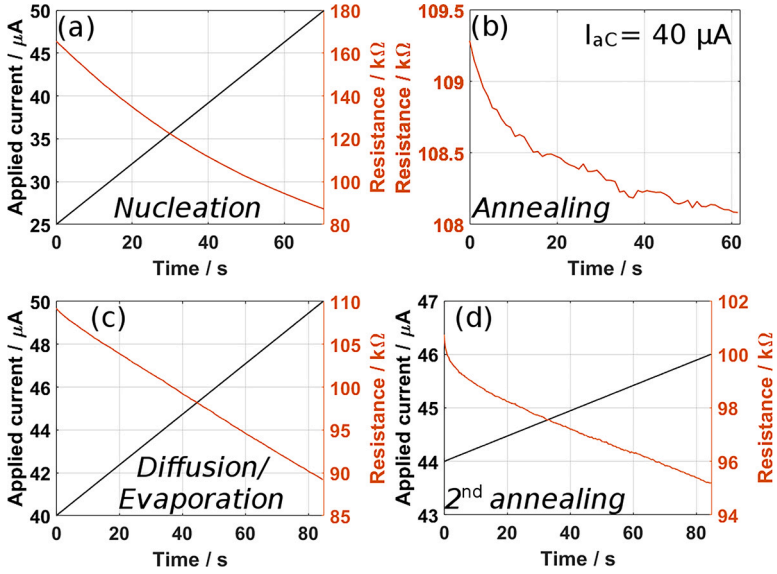

Fig. 3. Electrical measurements during the four main steps of the *in-situ* experiment. (a) Applied current and measured resistance over time of the current ramp in the nucleation step. (b) Resistance over time for a constant I_{aC} = 40 μA during the annealing step. (c) Applied current and measured resistance over time of the current ramp in the diffusion/evaporation step. (d) Applied current and measured resistance over time of the current ramp in the second annealing step.

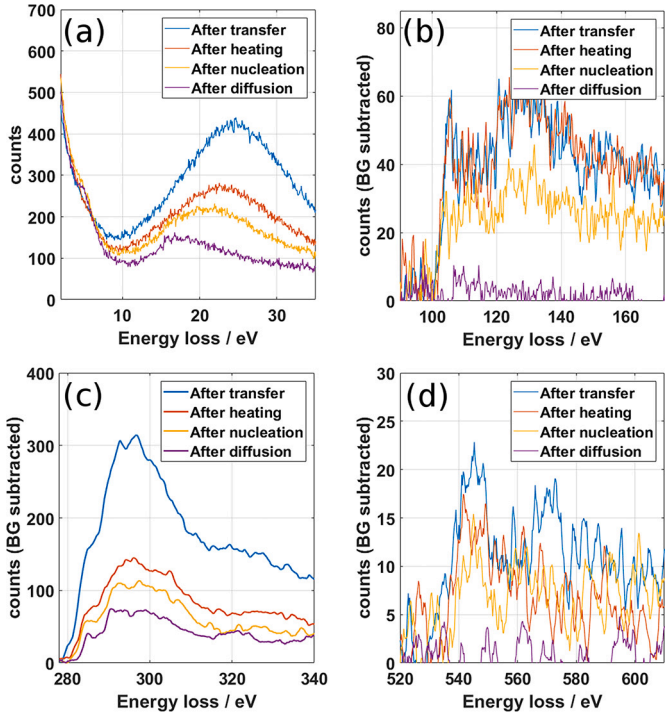

Fig. 4. EEL spectra acquired in TEM-diffraction mode at different stages of the experiment. (a) The low-loss region containing surface and bulk plasmon. (b-d) Background-corrected spectra of (b) the Si L edge, (c) the C K edge and (d) the O K edge. Acquisition times were (a) 0.001 s, (b) 0.1 s, (c) 0.3 s and (d) 0.5 s. Spectra in (c and d) have been smoothed by a moving-average filter over five pixels.

cation using core-loss EEL spectra indicates a concentration of 4 at% of Si, 14 at% of O and 82 at% of C (Fig. 4). Due to the low amount of Pt and the weak cross section (scattered intensity) of the O and N edges of Pt, quantification of the Pt concentration by EELS was not conducted. Implanted Ga could not be detected by EELS suggesting a concentration of less than 1 at%. It is noted that H will also be present but cannot be traced by EELS nor EDX.

It is of interest to compare the quantities of elements with high melting point (C, Si, Pt) in the initial state, as the specimen is exhibited to high temperatures during the *in-situ* experiment. C is the dominant contribution but EELS analysis indicates a considerable presence of Si (Si:C ≈ 1:20), which strongly outweighs Pt (Pt:Si < 1:25).

In the first step, the on-chip heating element was used to heat the sample up to approximately 250 °C to remove adsorbed species (H_2O, hydrocarbons) from the specimen. Fig. 5a shows a TEM image and SAED pattern of the aC nanofilm after the heating phase. They indicate that the nanofilm still possesses an amorphous structure. The PtC-cluster appear with slightly increased contrast, suggesting a slightly higher concentration of Pt atoms due to removal of hydrocarbons. EELS intensities indeed indicate a reduction of the C content by 40% and also the O content is reduced by 25%, while the Si contribution remains constant. The loss of C and O is attributed to desorption of hydrocarbons and water, respectively.

3.2. Nanoparticle nucleation

After pre-heating of the sample, electrical current ramps with increasing maximum current were applied to the sample. Up to I_{aC} = 25 μA ($1{\cdot}10^6$ Acm^{-2} in the central film area), no structural change could be observed. After the following current ramp up to I_{aC} = 50 μA ($2.6{\cdot}10^6$ Acm^{-2}) shown in Fig. 3a, several modifications of the sample are observed: The width of the aC nanofilm at its thinnest part decreases by 20 nm from 245 nm to 225 nm (Fig. 2b) and small NPs have formed. The EEL spectra show a rather homogeneous decrease of all the constituents (C, Si and O) by 35% (Fig. 4). The C K edge starts to show a more defined pre-peak related to π* bondings indicating a starting graphitization process (Fig. 4c). Furthermore, the Si L edge changes in shape with a shift of intensity from the peak at 105 eV to higher energies around 112 eV suggesting a structural change of the chemical bondings of the Si atoms (Fig. 4b).

Fig. 5 shows an analysis of the structure of the NPs. In comparison to the sub-nm sized amorphous Pt/C clusters homogeneously distributed over the aC nanofilm after pre-heating (Fig. 5a), the NP distribution is heterogeneous after the application of the current ramp up to 50 μA (Fig. 5c, d). The SAED pattern displayed in Fig. 5b was acquired from the central part of the film (as marked in Fig. 2b) and shows the two amorphous rings corresponding to the aC nanofilm and several small reflections linked to the NPs. The first three lattice distances of Pt fcc

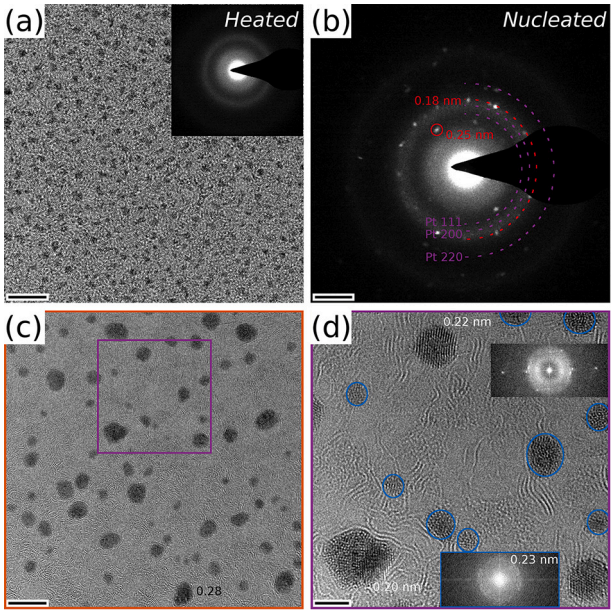

Fig. 5. Study of the NP nucleation: (a) TEM image of the central part of the sample before NP nucleation with inset SAED pattern (20x20 nm^{-2}) showing the amorphous nature of the specimen. (b) SAED pattern after NP nucleation acquired from green area in Fig. 2(b) showing two diffuse carbon rings and several reflections caused by the nucleated NPs. Pt rings are marked in purple and two spatial frequencies attributed to Si-based clusters in red. (c, d) HRTEM images show the heterogeneous appearance of the NPs with different sizes and lattice spacings only partially corresponding to Pt. Scale bars are (a, c) 9 nm, (b) 3 nm-1 and (d) 3 nm. Power spectra in (d) have a width of 25 nm^{-1}.

(Crystallography Open Database (COD) No 9008480) have been indicated in the SAED pattern and some of the reflections indeed correspond to these values. However, a strong contribution is observed at 0.25 nm distance and many reflections are visible at 0.18 nm, which cannot be attributed to pure Pt NPs. Instead, these values could correspond to the 120 (0.25 nm) and 020 (0.18 nm) lattice planes of PtSi (COD No 2106969). The lattice distance of 0.25 nm could also be linked to the 111 reflection of SiC (0.25 nm, COD No 9008856).

Fig. 5c and d show high-resolution TEM images of the NPs revealing their inhomogeneous size and structure distribution. Some NPs still possess sub-nm sizes while larger ones reach diameters of 6 nm and clearly exhibit faceted surfaces. When measuring lattice distances in the NPs and from the power spectrum, both Pt-fcc (111: 0.22 nm, 200: 0.196 nm) and PtSi (020: 0.28 nm) planes can be observed. In addition to the crystalline NPs, several amorphous NPs are visible, which have been marked by blue circles (Fig. 5d). When calculating a power spectrum selecting only these NPs (lower power spectrum in blue frame in Fig. 5d), a broader ring becomes visible. The ring is centered at 0.23 nm but extends to 0.25 and 0.21 nm, a range where quartz SiO_2 exhibits four lattice planes (110: 0.25 nm, 102: 0.23 nm, 111: 0.25 nm and 200: 0.21 nm, COD No 1011097). We therefore attribute the amorphous NPs to mostly SiO_2 with some incorporated Pt suggested by the darker spots in the inside of some of the NPs. Additionally, the graphitization of the aC nanofilm is seen in Figs. 5c and d, where several NPs, including the bigger NP in Fig. 5d, are partially covered by a graphitic layer.

Supplementary Movie S1 shows the evolution of the TEM images during the application of the current ramp and indicates that the NPs do not appear at every location at the same time. They are first observed at the borders of the central part of the film already below 40 μA and NPs are also largest at the border at the end of the step (Fig. 2b). Once a current of 45 μA is reached, NPs have appeared in the entire central area. It is noteworthy that once the NPs have formed at a specific place, the local NP arrangement on the film stays rather stable even though the applied current continues increasing. With increasing current, the NP also form in outer regions of the film. Together with the NP formation, the contrast of the film is reduced. This is linked to the observed material loss by EELS and can be explained by a densification and thinning process, as discussed below. The observed behavior during this step indicates that the process is step-like and once this process is completed, the situation stabilizes and only slower processes follow.

Several chemical processes happen during this phase, which we denominated as nucleation, as the formation of the crystalline Pt-based NPs from amorphous Pt-C clusters involves a phase transformation, typical for a nucleation process. This nucleation is accompanied by agglomeration and growth of the NPs. The exact sequence of the nucleation process is still in debate despite numerous studies on Pt NPs [32]. Here, the situation is different to typical chemical synthesis routes and more closely related to carbothermal shock heating approaches by Joule heating [11,14] as the specimen stays only for a few seconds at high temperature (Fig. 3a). Going in hand with the nucleation is the graphitization and densification of the aC nanofilm, likely assisted by the catalytic activity of Pt and Si, as well as the clustering of SiO_x and the incorporation of Si into the Pt NPs to form PtSi. Weakly bond C from the aC film and O released upon the incorporation of Si in the NPs can form CO_2 and evaporate, while the remaining C atoms form stronger and denser sp^2 bonds. Although not measurable by EELS, we assume that any Ga implantation has diffused out of the central area during this nucleation step due to its low melting point.

To give an estimation of the temperature, several previous studies from literature can be considered. Studies on PtSi NP formation under high vacuum from Pt thin films deposited on various Si-based substrates (crystalline Si, SiO_2, SiC, SiC+graphene) indicate a temperature of 800 °C necessary for PtSi formation [6,7]. As the SiO_x is not completely reduced, the temperature will be well below the onset temperature of about 1750 °C for direct carbothermal reduction of quartz at bulk scale [33]. Studies on catalytic graphitization by metals also indicate a temperature of between 750 and 850 °C [34,35], suggesting that the temperature reached in the nucleation phase will be in this temperature range. As SiC forms from carbon and silicon oxide at considerably higher temperatures above 1500 °C [36], its formation is discarded. Once the electrical current is switched off, the temperature rapidly decreases to room temperature, which represents a fast quenching of the specimens' state.

3.3. Nanoparticle annealing

After the nucleation phase, an annealing step at constant electrical current of I_{aC} = 40 μA (2.1 10^6 Acm^{-2}) was carried out. Supplementary movie S2 shows the evolution of the NPs during the annealing phase and Fig. 6 depicts the initial state (Fig. 6a), the first image after application of the electrical current (Fig. 6b) and the state after the complete annealing phase (Fig. 6c) without applied current. In both, initial and final image, the lattice fringes of the NPs are revealed, as also visible from the power spectra (Fig. 6d). A comparison of the reflections before and after the annealing step shows that the crystal structure of the NPs has changed, indicating a restructuring of the NPs. The corresponding lattice distances nevertheless correspond in both cases to either Pt or PtSi crystal structures: In Fig. 6a, lattice planes corresponding to the 021 (0.22 nm) orientation of PtSi and the 200 (0.20 nm) orientation of Pt can be identified and in Fig. 6c the orientations 101 (0.31 nm) and 111 (0.27 nm) of PtSi as well as again the 200 (0.20 nm) of Pt are visible.

The evolution from a large number of NPs with heterogeneous size distribution to a reduced number with larger diameters is clearly visible in the images. To emphasize this evolution, the NPs have been segmented into NPs with diameters below 2 nm (blue circles), between 2 and 4 nm (orange circles) and larger NPs (not marked). The number of each group of NPs is marked in the lower right corner of each image. The initial change upon application of I_{aC} is strong, leading to the almost complete disappearance of the smallest NPs and a considerable

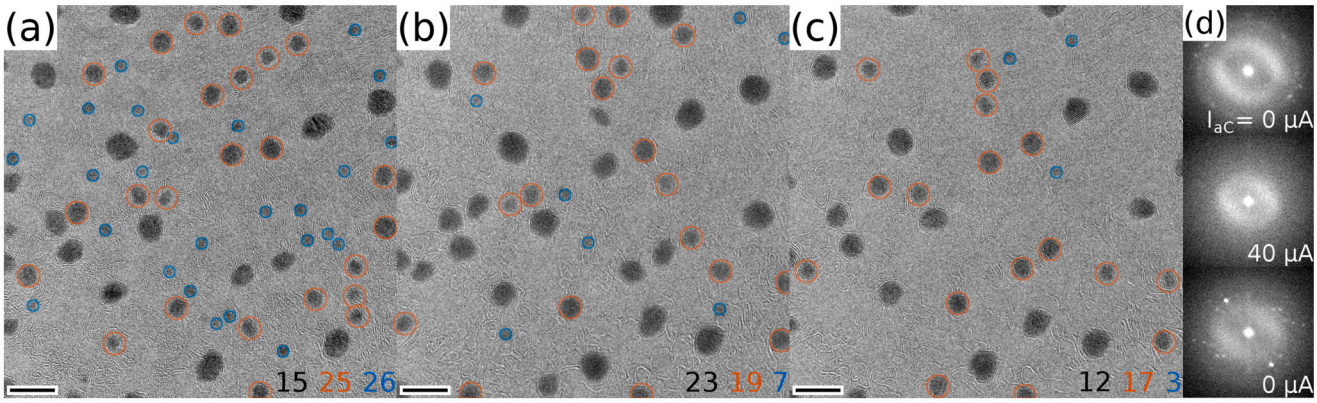

Fig. 6. Comparison of three TEM images (a) before, (b) at the start and (c) after the annealing phase with (d) the corresponding power spectra. NPs have been segmented into three different size classes: below 2 nm (blue), between 2 and 4 nm (orange) and above 4 nm (unmarked/black). The number of each class is indicated in the lower right corner. Scale bars are (a-c) 9 nm and the power spectra in (d) have a width of 12 nm^{-1}.

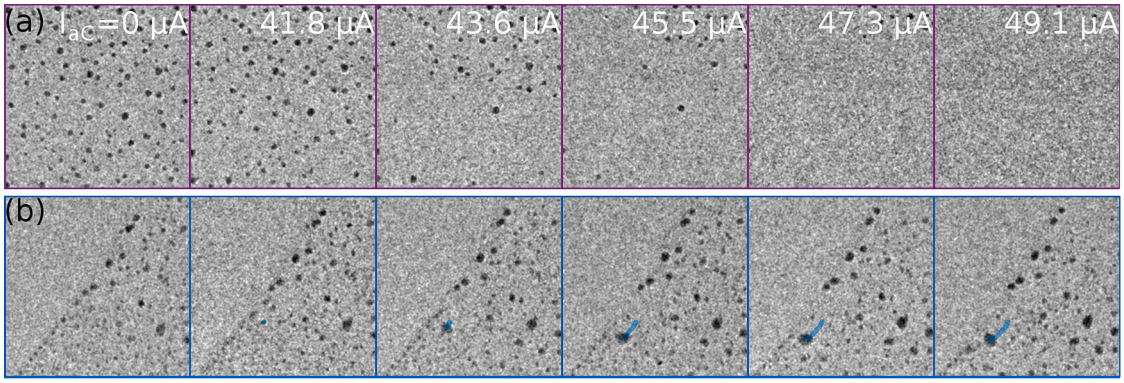

Fig. 7. Analysis of diffusion/evaporation step. Evolution of the TEM image appearance from (a) the central and (b) the lower area of the specimen as marked by respectively colored areas in Fig. 2c and d. The different currents applied during the images are indicated. Video sections have a width of 140 nm.

increase in number of the larger NPs. This strong change and rearrangement of the NPs can be partially linked to coalescence and Ostwald ripening processes. After this strong modification at the beginning of the electrical current application, the modification rate per image is reduced and only a few movements of entire NPs and uptakes of smaller NPs by larger ones can be observed (Supplementary movie S2). Moreover, as the total amount of NPs is decreasing throughout the sequence, a diffusion process out of the central region is observed, which happens more strongly in the next phase.

The strong modification in the NP arrangement seen in the first image with applied current is linked to the fast increase of the current directly to 40 µA, which can be seen as a thermal shock. This thermal shock stimulates the thermodynamical conditions for the observed fast Ostwald ripening and coalescence processes. During the buildup of the current flow, heat is generated fast and highly localized at sites posing barriers for the current flow, which can be different to the ones during the last application of electrical current. Once the flow is stabilized, the heat generation is more uniform and characteristic for a conventional annealing step.

In contrast to the clear imaging of lattice fringes before and after the annealing step, the high-resolution signal of the NPs is lost during the application of the electrical current and they appear with a more homogeneous dark contrast. This signal loss is not attributed to the electrical current itself or a related generated magnetic field as we have observed atomic resolution at much higher currents. Instead, it is attributed to the high sample temperature, a considerable fraction of the melting point of PtSi (1229 °C), which causes a strong phonon excitation leading to the smearing out of the lattice fringes in an image with an exposure time of 0.5 s.

The TEM images shown in Fig. 6 also give an insight in the interaction between NP and carbon support. Already before the annealing phase, several NPs are covered by graphitic planes, an observation which is even more true for the situation after the annealing, where all of the larger NPs are surrounded at least partially by one or even several graphite sheets. This graphitic encapsulation increases the stability of the NPs limiting their further rearrangement. The observation of an encapsulation is not surprising as Pt is well known as catalyst for graphene production. However, a graphitization is also observed in NP-free areas, e.g., in the lower left part of Fig. 6c.

In the central area, the processes happening during the annealing phase are thus the crystallization and growth of PtSi NPs and a continuing graphitization of the C nanofilm. A comparison of the TEM images of the whole film area before (Fig. 2b) and after (Fig. 2c) the annealing shows an additional shrinking of the film width by 25 nm to 200 nm. Moreover, the area with nucleated NPs has extended to a larger region of the film. As also observed in the next section, this further nucleation is different from the initial ones as NPs and clusters already nucleated in the central part start diffusing to outer areas and can act as nucleation centers.

3.4. Nanoparticle diffusion/evaporation

Fig. 7 gives an overview of the diffusion/evaporation phase, which consists in a current ramp from I_{aC} = 40 µA up to 50 µA (Fig. 3c). The TEM images before and after the diffusion/evaporation step (Fig. 2c and d) show that the central area of the film has been completely “cleaned” from the NPs. Supplementary movie S3 shows the evolution of the TEM image appearance at intermediate resolution and Fig. 7a and b shows

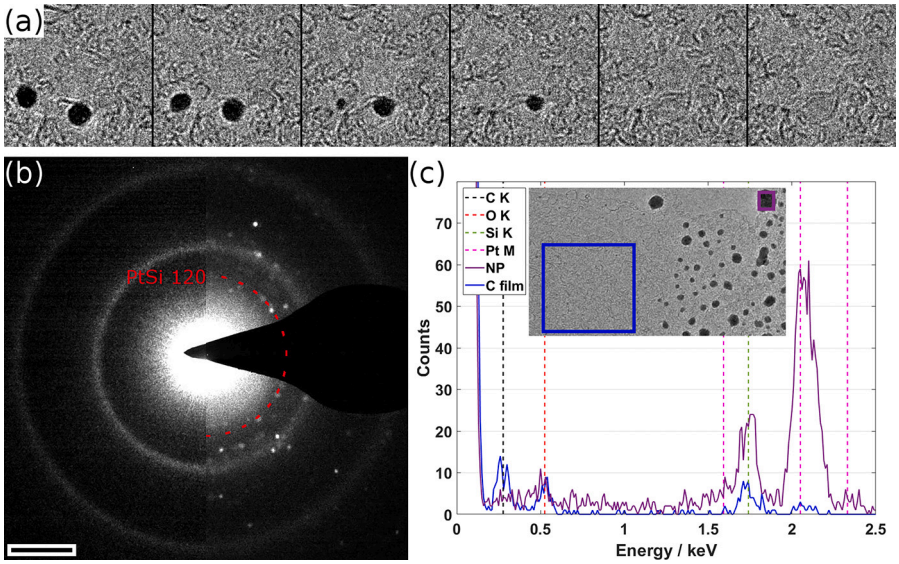

Fig. 8. Specimen analysis during and after the 2nd annealing phase. (a) TEM images acquired during the 2nd annealing phase. (b) Blend of two SAED patterns acquired of the NP-free film (left) and of a region with NPs. (c) EDX analysis of NP-free area (blue line and frame in (a)) and big NP (purple line and frame in (a)) acquired from areas marked in inset TEM image (height 100 nm). Scale bars are (b) 3 nm^{-1}.

excerpts of the movie from two specimen regions marked in Fig. 2. It can be observed that the NPs gradually disappear from the central area (Fig. 7a) and nucleate and grow in the outer regions (Fig. 7b).

EEL spectra acquired in the central area show that both Si and O are completely removed after the diffusion /evaporation phase. The intensity in the C edge is further reduced by 40%, leaving only 25% compared to the initial state. A further graphitization can be inferred from the analysis of the EEL spectra: the emerging plasmon peak at 6 eV (Fig. 4a) and the increasing prominence of the pre-peak at 285 eV in the C K edge (Fig. 4c).

Although the applied maximum current was the same as for the initial nucleation step (I_{aC} = 50 μA, Fig. 3a, c), the reduced thickness (3 nm) and width (195 nm) of the film cause a more than threefold increase of the current density to 8.5 10^6 Acm^{-2}). This increase in current density results in a further increase of the sample temperature, which leads to the complete disappearance of NPs in the central area of the film (Fig. 7a) and the shift of nucleation and growth of NPs to outer regions on both upper and lower side of the specimen (Figs. 7a and b). In Fig. 7b, the path of a NP is indicated by a blue line, after nucleation at I_{aC} = 41.8 μA. On its way, an Ostwald ripening process is observed, where the NP acts as nucleation center and takes up smaller clusters and its diameter grows from 3 nm to about 11 nm.

The fact that no apparent difference between upper and lower part of the film area can be observed indicates that electromigration only plays a minor role, as it would be linked to the direction of the electrical current. This shows that the electrical current flows through the nanofilm and that there is no direct interaction between the NPs and the electrical current.

While individual NPs diffuse entirely in the outer regions, the situation is different in the hotter, central part. A detailed look at the disappearance of the NPs in the central part (supplementary movie S3) shows that most of them first start to shrink in size before disappearing completely. This behavior is explained by a spatial confinement of those NPs by graphitic planes, as seen in Fig. 6, which reduces their mobility and inhibits their diffusion to colder, outer areas. Due to the increased current density, the temperature in the central part is further increased, leading to the evaporation of the confined PtSi nanoparticles. The vapor pressure curve of Pt indicates a temperature in the central part of above 1450 °C (at 10^{-7} mbar) [37], which is noteworthy, as such high temperatures cannot be obtained by conventional in-situ heating chips.

3.5. 2nd annealing phase

Following the current ramp of the diffusion/evaporation phase, another annealing step was conducted by employing a current ramp with a small increase from I_{aC} = 44 μA to 46 μA (Fig. 3d), while acquiring an image series of the central specimen area at higher magnification. Supplementary movie S4 shows this image series and Fig. 8a depicts several images of the series in the area marked by a frame in Fig. 2d. The following observations can be made: The C network remains almost completely stable during this annealing step except in the lower part, where three larger NP are evaporated and continuously shrink in size, leaving graphene sheets behind. Two of these NPs are visible in Fig. 8a. Another NP in the central part disappears within a single frame while yet another stays completely stable throughout the series. This again illustrates the importance of the interaction between NP and substrate.

Fig. 8b shows a SAED pattern obtained from a NP-free carbon film as marked in Fig. 2d in comparison to a SAED pattern acquired from a region with NPs (right side of Fig. 8b). The two rings corresponding to the carbon structure have strongly sharpened indicating an untextured graphitic structure. This graphitized nanofilm remains stable under ambient conditions and could thus be reused at this stage for a similar study by deliberately depositing, e.g., precursor molecules or metal salts on the film. The reflections visible in the pattern acquired from carbon film + NPs can be attributed to PtSi, with the 120 lattice distance (0.25 nm) exemplary marked, confirming thus the alloyed structure of the NPs.

3.6. Electrical properties

As the heating is performed by Joule heating induced by electrical current, the resistance of the specimen is monitored during the experiment. The resistance is measured in a two-probe setup and includes the contacts and the whole aC nanofilm. The central part possesses the thinnest width and will therefore be a significant contribution to the measured resistance. Figure S3 in the SI shows two electrical measurements at low currents conducted after heating and after the diffusion/evaporation step. The resistance after heating is 800 kΩ, which can be approximately separated into the central part (600 kΩ) and the outer, wider parts of the sample (200 kΩ) by geometrical analysis of the sample (Figure S3). The contact resistance is typically in the range of 150 Ω and is thus only a negligible contribution to the overall resistance.

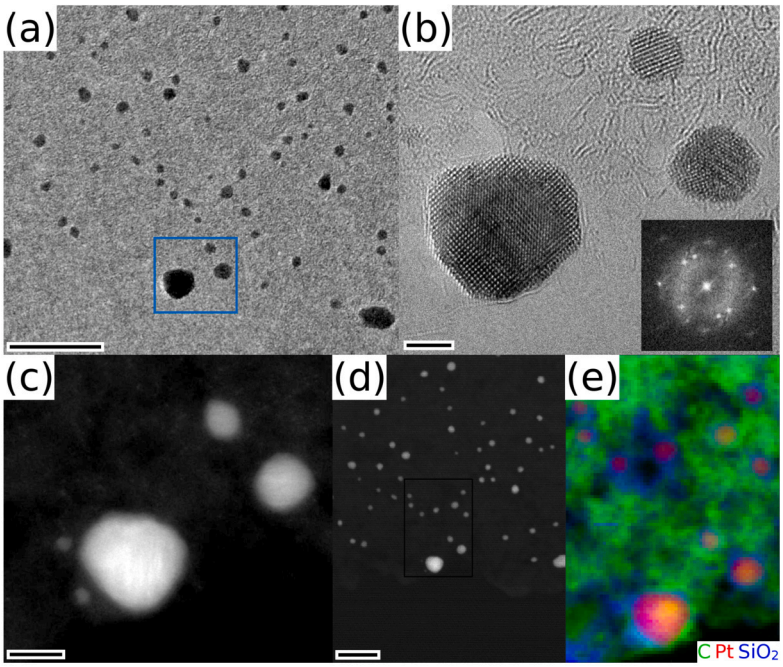

Fig. 9. TEM and STEM-EELS analysis of NPs obtained from a similar specimen and *in-situ* experiment. (a) TEM image of NPs on a carbon nanofilm nucleated and grown during *in-situ* application of electrical current. (b) HRTEM image of the three NPs marked in (a) with inset power spectrum (width 14 nm^{-1}). (c) HAADF-STEM image of the identical specimen area after contact to air showing a separation of two small NPs from the large NP. The contrast of the image has been adjusted non-linearly to visualize both Pt-based NPs and the carbon support. (d) DF-STEM image at lower magnification with the area selected for spectrum imaging marked. (e) Chemical spectrum image obtained from factorization showing the C (green), Pt (red) and SiO_2 (blue) contributions. Scale bars are (a) 30 nm, (b) 3 nm, (c) 5 nm and (d) 20 nm.

A look at the evolution of the resistance during the nucleation and annealing phases shows a strong decrease to less than 100 kΩ during the nucleation phase (Fig. 3a), while basically remaining constant during the annealing phase at a constant I_{aC} = 40 μA, showing only a minor decay of less than 1% (Fig. 3b). The decrease during the nucleation phase is attributed to the graphitization of the aC nanofilm and to the increasing film temperature, which causes an improvement of the semiconducting nanofilms' conductance. The trend is similar for the following phases (Fig. 3c, d) with the lowest resistance of less than 90 kΩ measured at I_{aC} = 50 μA at the end of the diffusion/evaporation step. A comparison between initial and final state is given by the measurements at low currents (Figure S3), which shows a resistivity of 350 kΩ after the diffusion/evaporation phase, indicating a strong increase of the conductivity due to the graphitization in the central part. The electrical measurements and resulting analysis of the conductivity of the aC nanofilm will be discussed in more detail in a later article. However, the observed transitions in the electrical measurements at high currents are smooth, suggesting that the NP nucleation and annealing has no effect on the electrical conductivity.

3.7. Chemical analysis

To confirm the composition of the NPs, STEM-EDX and EELS analyses were performed in another microscope after the *in-situ* experiment. Fig. 8c shows the comparison of two EDX spectra acquired from the NP-free region of the carbon nanofilm (blue line and frame in inset TEM image) and from the large NP (purple line and frame). While carbon is the major contribution in the NP-free region (75 at%), a considerable amount of silicon dioxide (25 at%) is found as well. In the NP region, Pt (36 at%) and Si (37 at%) are found in equal parts confirming a PtSi structure. The oxygen content (16 at%) suggests a partial oxidation of the Si at the NPs' surface caused by the contact to air between the *in-situ* experiment and the analytical studies. Ga could not be detected indicating that any implanted ions have diffused out of the investigated area.

Fig. 9 shows the analysis of NPs formed on a carbon nanofilm during an additional, similar *in-situ* experiment performed with the specimen described in Figure S2 (SI). A TEM image after the nucleation phase again shows a rather inhomogeneous size distribution with smaller NPs on the film and larger NPs at its edge (Fig. 9a). The crystalline structure of the NPs is analyzed by HRTEM (Fig. 9b), where the lattice planes of the big NP fit to PtSi (020: 0.28 nm and 220: 0.20 nm) and the small show contributions from both Pt-fcc (111: 0.23 nm) and PtSi (200: 0.30 nm). This experiment was stopped after the nucleation of PtSi NPs to perform spatially-resolved EELS analysis in the probe-corrected microscope and the specimen was in contact to air during the sample transfer. This led to a separation of two small NPs from the larger one (Fig. 9c). STEM-EELS data was acquired from a larger region and a non-negative matrix factorization was conducted to determine the different contributions as the EELS signal of Pt in the investigated energy range is weak. The spectral data could be separated into three factors, which were identified to correspond to the carbon substrate, Pt and SiO_2 (details in the SI, Figures S4-S7). The resulting chemical map is shown in Fig. 9e and reveals that all the NPs, including the small ones, contain Pt as well as contributions from SiO_2, in many cases in the form of a shell. This analysis confirms the formation of PtSi NPs, which however oxidize and de-alloy at ambient conditions.

4. Conclusion

The *in-situ* transmission electron microscopy (TEM) experiment based on Joule heating induced by the application of electrical currents shows that PtSi nanoparticles (NPs) are synthesized on an amorphous carbon (aC) nanofilm. The NPs form from SiO_x residues (4 at%) stemming from the mica substrate used for the preparation of the aC nanofilm and hydrocarbonated Pt molecules (<1 at%) deposited by secondary electrons/ions generated during the transfer of the specimen to the *in-situ* microchip. Nucleation of Pt NPs is accompanied by incorporation of Si and a graphitization and densification of the C nanofilm. The NPs crystallize and grow during an annealing step and start diffusing

out of the hot central area of the film, where graphitization continues. The graphitized film was found to be stable under ambient conditions after the *in-situ* experiment, while the PtSi NPs partially oxidize after contact with air.

The presented experiment illustrates the possibility of performing synthesis and NP dynamics experiments by *in-situ* TEM at high spatial resolution and high temperatures using a carbon nanofilm as support and heat source. The experiments are facilitated by a recently developed support-based sample transfer and contacting allowing to minimize damage and contamination [28]. Although demonstrated here with contamination material, a deliberate preparation with numerous and various precursors is possible.

Control over the process is given by the electrical current, with the critical value being the current density in the part of the aC nanofilm with minimum cross section. The threshold for initiation of structural changes in the sample was approximately $2{\cdot}10^6$ Acm^{-2}. The approach is also compatible with studies of carbothermal shock synthesis methods by the application of electrical current pulses.

CRediT authorship contribution statement

Simon Hettler: Writing – review & editing, Writing – original draft, Methodology, Investigation, Formal analysis, Data curation, Conceptualization. **Raul Arenal:** Writing – review & editing, Funding acquisition, Supervision.

Declaration of competing interest

The authors declare that they have no known competing financial interests or personal relationships that could have appeared to influence the work reported in this paper.

The author (R.A.) is an Editorial Board Member and Guest Editor for Carbon Trends and was not involved in the editorial review or the decision to publish this article.

Data availability

Data will be made available on request.

Acknowledgements

The authors acknowledge funding from the European Union's Horizon 2020 research and innovation programme under the Marie Sklodowska-Curie grant agreement No 889546 and by the Spanish MICIU (PID2019-104739GB-100/AEI/10.13039/501100011033) as well from the Gobierno de Aragón (DGA) under project E13-23R. The microscopy works have been conducted in the Laboratorio de Microscopias Avanzadas (LMA) at Universidad de Zaragoza.

Appendix A. Supplementary material

Supplementary material related to this article can be found online at https://doi.org/10.1016/j.cartre.2024.100348.

References

[1] K.D. Gilroy, A. Ruditskiy, H.-C. Peng, D. Qin, Y. Xia, Bimetallic nanocrystals: syntheses, properties, and applications, Chem. Rev. 116 (18) (2016) 10414–10472, https://doi.org/10.1021/acs.chemrev.6b00211.

[2] A. Wong, Q. Liu, S. Griffin, A. Nicholls, J.R. Regalbuto, Synthesis of ultrasmall, homogeneously alloyed, bimetallic nanoparticles on silica supports, Science 358 (6369) (2017) 1427–1430, https://doi.org/10.1126/science.aao6538.

[3] J.-W. Yeh, S.-K. Chen, S.-J. Lin, J.-Y. Gan, T.-S. Chin, T.-T. Shun, C.-H. Tsau, S.-Y. Chang, Nanostructured high-entropy alloys with multiple principal elements: novel alloy design concepts and outcomes, Adv. Eng. Mater. 6 (5) (2004) 299–303, https://doi.org/10.1002/adem.200300567.

[4] P.-C. Chen, X. Liu, J.L. Hedrick, Z. Xie, S. Wang, Q.-Y. Lin, M.C. Hersam, V.P. Dravid, C.A. Mirkin, Polyelemental nanoparticle libraries, Science 352 (6293) (2016) 1565–1569, https://doi.org/10.1126/science.aaf8402.

[5] S. Gao, S. Hao, Z. Huang, Y. Yuan, S. Han, L. Lei, X. Zhang, R. Shahbazian-Yassar, J. Lu, Synthesis of high-entropy alloy nanoparticles on supports by the fast moving bed pyrolysis, Nat. Commun. 11 (1) (2020) 2016, https://doi.org/10.1038/s41467-020-15934-1.

[6] J. Zhu, G.A. Somorjai, Formation of platinum silicide on a platinum nanoparticle array model catalyst deposited on silica during chemical reaction, Nano Lett. 1 (1) (2001) 8–13, https://doi.org/10.1021/nl005512q.

[7] K. Idczak, S. Owczarek, L. Markowski, Platinum silicide formation on selected semiconductors surfaces via thermal annealing and intercalation, Appl. Surf. Sci. 572 (29) (2022) 151345, https://doi.org/10.1016/j.apsusc.2021.151345.

[8] X. Chen, X.-B. Wang, S. Han, D. Wang, C. Li, W. Guan, W.-Y. Li, C. Liang, Overcoming limitations in the strong interaction between pt and irreducible sio2 enables efficient and selective hydrogenation of anthracene, ACS Appl. Mater. Interfaces 14 (1) (2022) 590–602, https://doi.org/10.1021/acsami.1c16965.

[9] X. Chen, C. Liang, Transition metal silicides: fundamentals, preparation and catalytic applications, Catal. Sci. Technol. 9 (18) (2019) 4785–4820, https://doi.org/10.1039/C9CY00533A.

[10] D. Zhang, B. Gökce, S. Barcikowski, Laser synthesis and processing of colloids: fundamentals and applications, Chem. Rev. 117 (5) (2017) 3990–4103, https://doi.org/10.1021/acs.chemrev.6b00468.

[11] Y. Yao, Z. Huang, P. Xie, S.D. Lacey, R.J. Jacob, H. Xie, F. Chen, A. Nie, T. Pu, M. Rehwoldt, D. Yu, M.R. Zachariah, C. Wang, R. Shahbazian-Yassar, J. Li, L. Hu, Carbothermal shock synthesis of high-entropy-alloy nanoparticles, Science 359 (6383) (2018) 1489–1494, https://doi.org/10.1126/science.aan5412.

[12] R. Jiang, Y. Da, X. Han, Y. Chen, Y. Deng, W. Hu, Ultrafast synthesis for functional nanomaterials, Cell Rep. Phys. Sci. 2 (1) (2021) 100302, https://doi.org/10.1016/j.xcrp.2020.100302.

[13] A. Abdelhafiz, B. Wang, A.R. Harutyunyan, J. Li, Carbothermal shock synthesis of high entropy oxide catalysts: dynamic structural and chemical reconstruction boosting the catalytic activity and stability toward oxygen evolution reaction, Adv. Energy Mater. 12 (35) (2022) 97166, https://doi.org/10.1002/aenm.202200742.

[14] W. Shi, Z. Li, Z. Gong, Z. Liang, H. Liu, Y.-C. Han, H. Niu, B. Song, X. Chi, J. Zhou, H. Wang, B.Y. Xia, Y. Yao, Z.-Q. Tian, Transient and general synthesis of high-density and ultrasmall nanoparticles on two-dimensional porous carbon via coordinated carbothermal shock, Nat. Commun. 14 (1) (2023) 7350, https://doi.org/10.1038/s41467-023-38023-5.

[15] Y.-C. Han, J. Yi, B. Pang, N. Wang, X.-C. Li, T. Yao, K.S. Novoselov, Z.-Q. Tian, Graphene-confined ultrafast radiant heating for high-loading subnanometer metal cluster catalysts, Nat. Sci. Rev. 10 (6) (2023) nwad081, https://doi.org/10.1093/nsr/nwad081.

[16] Z. Huang, Y. Yao, Z. Pang, Y. Yuan, T. Li, K. He, X. Hu, J. Cheng, W. Yao, Y. Liu, A. Nie, S. Sharifi-Asl, M. Cheng, B. Song, K. Amine, J. Lu, T. Li, L. Hu, R. Shahbazian-Yassar, Direct observation of the formation and stabilization of metallic nanoparticles on carbon supports, Nat. Commun. 11 (1) (2020) 6373, https://doi.org/10.1038/s41467-020-20084-5.

[17] W. Dachraoui, T.R. Henninen, D. Keller, R. Erni, Multi-step atomic mechanism of platinum nanocrystals nucleation and growth revealed by in-situ liquid cell stem, Sci. Rep. 11 (1) (2021) 131, https://doi.org/10.1038/s41598-021-03455-w.

[18] W. Gao, A.O. Elnabawy, Z.D. Hood, Y. Shi, X. Wang, L.T. Roling, X. Pan, M. Mavrikakis, Y. Xia, M. Chi, Atomistic insights into the nucleation and growth of platinum on palladium nanocrystals, Nat. Commun. 12 (1) (2021) 744, https://doi.org/10.1038/s41467-021-23290-x.

[19] L. Wang, L. Wang, X. Meng, F.-S. Xiao, New strategies for the preparation of sinter–resistant metal–nanoparticle–based catalysts, Adv. Mater. 31 (50) (2019), https://doi.org/10.1002/adma.201901905.

[20] H. Tabassum, A. Mahmood, B. Zhu, Z. Liang, R. Zhong, S. Guo, R. Zou, Recent advances in confining metal-based nanoparticles into carbon nanotubes for electrochemical energy conversion and storage devices, Energy Environ. Sci. 12 (10) (2019) 2924–2956, https://doi.org/10.1039/C9EE00315K.

[21] K. Kanaya, H. Kawakatsu, K. Itō, H. Yotsumoto, Experiment on the electron phase microscope, J. Appl. Phys. 29 (7) (1958) 1046–1049, https://doi.org/10.1063/1.1723360.

[22] R. Danev, K. Nagayama, Transmission electron microscopy with Zernike phase plate, Ultramicroscopy 88 (4) (2001) 243–252, https://doi.org/10.1016/S0304-3991(01)00088-2.

[23] L. Grünewald, D. Gerthsen, S. Hettler, Fabrication of phase masks from amorphous carbon thin films for electron-beam shaping, Beilstein J. Nanotechnol. 10 (2019) 1290–1302, https://doi.org/10.3762/bjnano.10.128.

[24] M. Malac, S. Hettler, M. Hayashida, E. Kano, R.F. Egerton, M. Beleggia, Phase plates in the transmission electron microscope: operating principles and applications, Microscopy 70 (1) (2021) 75–115, https://doi.org/10.1093/jmicro/dfaa070.

[25] S. Hettler, R. Arenal, Aberration-corrected transmission electron microscopy with Zernike phase plates, Ultramicroscopy 239 (2022) 113564, https://doi.org/10.1016/j.ultramic.2022.113564.

[26] S. Hettler, E. Kano, M. Dries, D. Gerthsen, L. Pfaffmann, M. Bruns, M. Beleggia, M. Malac, Charging of carbon thin films in scanning and phase-plate transmission electron microscopy, Ultramicroscopy 184 (Pt A) (2018) 252–266, https://doi.org/10.1016/j.ultramic.2017.09.009.

[27] S. Hettler, D. Sebastian, M. Pelaez-Fernandez, A.M. Benito, W.K. Maser, R. Arenal, In-situ reduction by Joule heating and measurement of electrical conductivity of

graphene oxide in a transmission electron microscope, 2D, Materials 8 (3) (2021) 031001, https://doi.org/10.1088/2053-1583/abedc9.
[28] S. Hettler, M. Furqan, R. Arenal, Support-based transfer and contacting of individual nanomaterials for in situ nanoscale investigations, Small Methods (2024) 2400034, https://doi.org/10.1002/smtd.202400034.
[29] R.F. Egerton, Electron Energy-Loss Spectroscopy in the Electron Microscope, 3rd edition, Springer Science+Business Media LLC, Boston, MA, 2011.
[30] M. Huth, F. Porrati, C. Schwalb, M. Winhold, R. Sachser, M. Dukic, J. Adams, G. Fantner, Focused electron beam induced deposition: a perspective, Beilstein J. Nanotechnol. 3 (2012) 597–619, https://doi.org/10.3762/bjnano.3.70.
[31] B. Bhattarai, A. Pandey, D.A. Drabold, Evolution of amorphous carbon across densities: an inferential study, Carbon 131 (2018) 168–174, https://doi.org/10.1016/j.carbon.2018.01.103.
[32] J. Quinson, K.M.Ø. Jensen, From platinum atoms in molecules to colloidal nanoparticles: a review on reduction, nucleation and growth mechanisms, Adv. Colloid Interface Sci. 286 (2020) 102300, https://doi.org/10.1016/j.cis.2020.102300.
[33] K. Yasuda, T. Nohira, Electrochemical production of silicon, High Temp. Mater. Process. 41 (1) (2022) 247–278, https://doi.org/10.1515/htmp-2022-0033.
[34] J. Nam, D.-C. Kim, H. Yun, D.H. Shin, S. Nam, W.K. Lee, J.Y. Hwang, S.W. Lee, H. Weman, K.S. Kim, Chemical vapor deposition of graphene on platinum: growth and substrate interaction, Carbon 111 (1) (2017) 733–740, https://doi.org/10.1016/j.carbon.2016.10.048.
[35] S. Khoshk Rish, A. Tahmasebi, R. Wang, J. Dou, J. Yu, Formation mechanism of nano graphitic structures during microwave catalytic graphitization of activated carbon, Diam. Relat. Mater. 120 (2021) 108699, https://doi.org/10.1016/j.diamond.2021.108699.
[36] A.S. Vlasov, A.I. Zakharov, O.A. Sarkisyan, N.A. Lukasheva, Obtaining silicon carbide from rice husks, Refractories 32 (9–10) (1991) 521–523, https://doi.org/10.1007/BF01287542.
[37] A.S. Darling, The vapour pressures of the platinum metals, Platin. Met. Rev. 8 (4) (1964) 134–140, https://doi.org/10.1595/003214064X84134140.